

Northumbria Research Link

Citation: Xue, Yuanlin, Chen, Wenge, Wang, Jiaojiao, Dong, Longlong, Zhao, Qian and Fu, Yong Qing (2018) Formation Mechanism and Cohesive Energy Analysis of Metal-coated Graphene Nanocomposites Using In-situ Co-reduction Method. *Materials*, 11 (11). p. 2071. ISSN 1996-1944

Published by: MDPI

URL: <https://doi.org/10.3390/ma11112071> <<https://doi.org/10.3390/ma11112071>>

This version was downloaded from Northumbria Research Link:
<http://nrl.northumbria.ac.uk/id/eprint/36351/>

Northumbria University has developed Northumbria Research Link (NRL) to enable users to access the University's research output. Copyright © and moral rights for items on NRL are retained by the individual author(s) and/or other copyright owners. Single copies of full items can be reproduced, displayed or performed, and given to third parties in any format or medium for personal research or study, educational, or not-for-profit purposes without prior permission or charge, provided the authors, title and full bibliographic details are given, as well as a hyperlink and/or URL to the original metadata page. The content must not be changed in any way. Full items must not be sold commercially in any format or medium without formal permission of the copyright holder. The full policy is available online: <http://nrl.northumbria.ac.uk/policies.html>

This document may differ from the final, published version of the research and has been made available online in accordance with publisher policies. To read and/or cite from the published version of the research, please visit the publisher's website (a subscription may be required.)



**Northumbria
University**
NEWCASTLE



UniversityLibrary

1 *Type of the Paper (Article)*

2 **Formation Mechanism and Cohesive Energy Analysis** 3 **of Metal-coated Graphene Nanocomposites Using** 4 ***In-situ* Co-reduction Method**

5 Yuanlin Xue ¹, Wenge Chen ^{1,*}, Jiaojiao Wang ¹, Longlong Dong ^{2,*}, Qian Zhao ¹ and YongQing Fu
6 ^{3,*}

7 ¹ School of Materials Science and Engineering, Xi'an University of Technology, Xi'an, PR China;
8 xueyuanlinxyl@163.com, wjxaut@126.com, 1905238526@qq.com

9 ² Advanced Materials Research Central, Northwest Institute for Nonferrous Metal Research, Xi'an, PR China;
10 donglong1027@163.com

11 ³ Faculty of Engineering and Environment, Northumbria University, Newcastle upon Tyne, UK;
12 richard.fu@northumbria.ac.uk

13 * Correspondence: wgchen001@263.net; donglong1027@163.com; richard.fu@northumbria.ac.uk; Tel.:
14 +86-29-82312383

15 **Abstract:** Nanocomposite powders based on metal-coated graphene were synthesized using an
16 *in-situ* co-reduction method in order to improve wettability and interfacial bonding between
17 graphene and metal. Graphene oxide (GO) of 2~3 atomic layers was synthesized using the
18 Hummer's method with graphite as a raw material, and then dispersed into a dispersing agent
19 solution mixed with *N*-Methyl pyrrolidone and deionized water to form a homogeneous GO
20 suspension, which was finally added into electroless plating solutions for the reduction process.
21 Copper-coated graphene (Cu@graphene) and nickel-coated graphene (Ni@graphene) were
22 synthesized using this one-step and co-reduction method by mixing salt solutions containing metal
23 ions and GOs into the plating solution. The copper ions or nickel ions were adsorbed and bonded
24 onto the edges and surfaces of graphene, which was reduced from the GOs using a strong reducing
25 agent of ascorbic acid or sodium borohydride. Crystalline copper particles with an average size of
26 about 200 nm were formed on the surface of graphene, whereas amorphous or nanocrystalline
27 nickel particles with an average size of 55 nm were formed on the surface of graphene. Distribution
28 of these metal particles on the graphene is homogeneous and highly dispersed, which can
29 effectively improve the sinterability of composite powders. Cohesive energy distribution between
30 graphene and metal interface was analyzed using first-principle calculation method. Formation
31 mechanism of metal coated graphene was identified to be that both the GO and metal ions were
32 simultaneously reduced in the reducing agents, and thus a strong chemical bonding of
33 graphene/metal was formed between the metal particles and graphene.

34 **Keywords:** graphene, coated metals, preparation, characterization, mechanisms

35 **1. Introduction**

36 Graphene has excellent physical and mechanical properties owing to its unique structure [1]. In
37 fact, graphene of 2~3 atomic layers shows good electrical performance [2]; graphene of 6~7 atomic
38 layers exhibits a remarkable thermal characteristic [3]; and graphene of about 10 atomic layers
39 possesses outstanding mechanical properties [4]. These excellent properties make graphene one of
40 the most promising materials for wide-range applications, including nano-electronics, composite
41 materials, catalysts, sensors, energy storage, transistors, touch screens, and gene sequencing, etc
42 [5-9].

43 Graphene is commonly used as a reinforcing material in composites, including metal, polymer
44 and ceramic matrix composites [10-14]. However, its difficulty of uniform dispersion into the matrix,

45 poor wettability to many substrate materials and poor interfacial bonding with matrix seriously
46 restrict its successful applications in composite materials. One of the critical issues is how to
47 improve its interfacial bonding with the metal matrix in order to efficiently transfer the applied load
48 and enhance electron/heat transport. It is critical to find solutions to uniformly disperse the
49 graphene nanoflakes as an efficient reinforce agent and avoid their agglomeration.

50 An efficient method was proposed to pre-coat the surface of graphene with a layer of metal in
51 order to prevent its agglomeration in the matrix [15,16]. Due to the improved dispersion and good
52 interfacial bonding, thermal energy and electrons can be effectively transferred between graphene
53 and the coated metal, and thus the wettability of metal-coated graphene can be significantly
54 improved. The so-formed metal coated graphene composite powders (in this paper we will use
55 metal@graphene) will maintain good properties of both graphene and metal, and could find
56 wide-range applications in the fields of energy, catalysis, biomedicine, sensors and spectroscopy.
57 There are extensive studies to synthesize various types of metal@graphene composites, using
58 solvothermal method, cation exchange, thermal exfoliation, chemical vapor deposition, etc [17-21].
59 Hassan et al. [22] prepared uniform and well-dispersed metallic nanoparticles on chemically
60 converted graphene sheets using a chemical reduction method assisted by microwave irradiation.
61 Wang et al. [23] fabricated Ni-graphene nanocomposites using a multi-step electroless deposition,
62 and Ni nanoparticles with an average diameter of 20 nm were decorated onto reduced graphene
63 oxide (rGO) sheets. Kuang et al. [24] prepared Ni/graphene composites using an electro-deposition
64 with GO sheets mixed inside a nickel sulfamate solution, and graphene in the composites was
65 reduced from the GO sheets during an electro-deposition process. Cao et al. [25] synthesized
66 Ni/graphene nanocomposites using a chemical vapor deposition approach. As reported in the
67 literature, the commonly used methods for preparing metal@graphene are focused mainly on
68 chemical synthesis methods, however, these are often multi-step and high cost processes.

69 Therefore, in the present work, we synthesized Cu@graphene and Ni@graphene using a new
70 and efficient *in-situ* co-reduction method. The formation mechanism of the metal@graphene
71 composite was analyzed based on various characterization results. The cohesive energy between
72 metal and graphene was calculated and analyzed using the first principle calculation method.

73 2. Materials and Methods

74 2.1. Raw materials

75 In this work, the raw materials used were flakes of graphite powders (200 mesh, 99.90% purity,
76 Nanjing Xian Feng Nano Materials Technology Co. Ltd. Jiangsu, China). Chemical reagents, such as
77 copper sulfate, nickel sulfate, sodium hydroxide, concentrated sulfuric acid (98%), HCl (37%), H₂O₂
78 (30%), *N*-methyl pyrrolidone, NaOH (PH=11), ammonia (25-28%), KMnO₄, were bought from
79 Sinopharm Chemical Reagent Co. Ltd. Shanghai, China. All the chemicals were used directly
80 without further purification.

81 2.2. Fabrication of graphene oxide (GO)

82 The standard Hummer's method was employed to synthesize GO [21,26,27]. A typical
83 experiment can be summarized as follows: (a) 5 g of graphite powder was mixed with 115 mL
84 concentrated H₂SO₄ and then stirred using an ice-bath (at 0 °C) for 30 min; (b) At room temperature
85 of 25 °C, 20 g of KMnO₄ was slowly added into the above mixture and agitated for 120 min; (c) The
86 temperature of above mixture solution was increased to 35 °C during the process; and then 50 mL

87 of deionized water (DI) was gradually added into the above solution; (d) 80 mL of DI water was
 88 gradually added into the system; After all the reactions were completed, hydrogen peroxide (30
 89 wt%) was added into the solution until it turned into a yellow color and no bubbles were further
 90 produced; (e) The mixture was filtered and washed using HCl (5 wt%) and DI water for ~28 times,
 91 and then dried at 70 °C for 12 hours using a vacuum freeze-drying method. In this paper, we did
 92 not perform the recycling of the residual product as reported in Ref [28], but this will be explored in
 93 the future work.

94 2.3. Fabrication of metal-coated graphene (metal@graphene) nanocomposites powders

95 As illustrated in Figure 1, metal@graphene powders were prepared using a thermo-electroless
 96 plating method. The compositions of the metal plating solutions (Cu or Ni) and reaction conditions
 97 are listed in Table 1.

98 **Table 1.** The compositions of metal plating solution (Cu or Ni) and reaction conditions.

| Plating solution | Chemical | Function | Concentration |
|------------------|--------------------------------------|---------------------|-------------------------|
| Copper | CuSO ₄ ·5H ₂ O | Source Cu | 50 g·L ⁻¹ |
| | PVP | surfactant agent | 0.4 mg·mL ⁻¹ |
| | Ascorbic | Reducing agent | 2 g·L ⁻¹ |
| | NaOH | Adjust the pH value | 50 g·L ⁻¹ |
| Nickel | NiSO ₄ ·6H ₂ O | Source Ni | 1.3 g·L ⁻¹ |
| | PVP | surfactant agent | 0.4 mg·mL ⁻¹ |
| | NaBH ₄ | Reducing agent | 8 g·L ⁻¹ |
| | NH ₃ ·H ₂ O | Adjust the pH value | 25-28 wt% |

99

100 The detailed electroless plating processes are listed as follows:

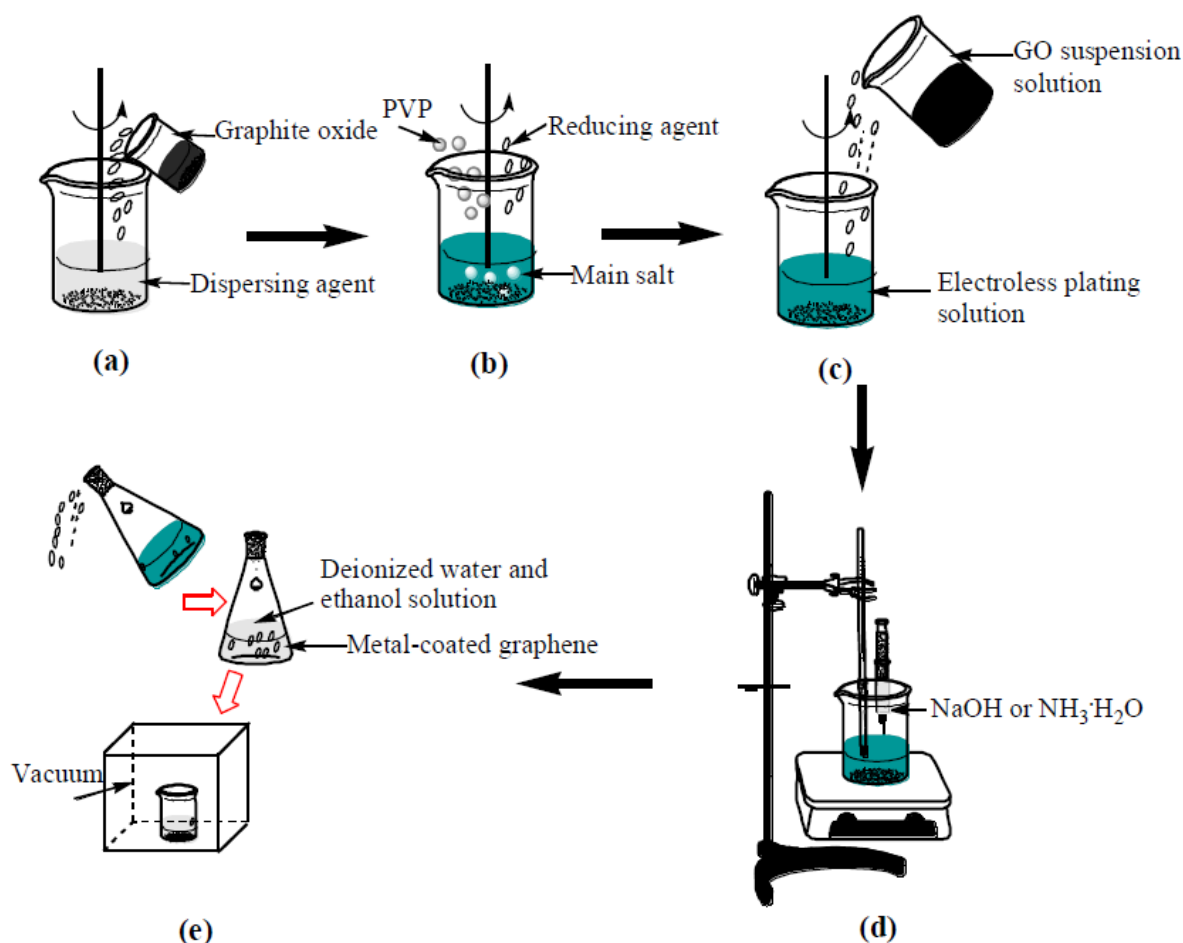
101 (a) 20 mg of GO was dispersed into 100 mL dispersing agent solution in an ultrasound bath for
 102 3 hours to obtain a homogeneous GO suspension solution (0.2 mg/mL) as shown in Figure 1(a). The
 103 dispersing agent in the copper plating and nickel plating are *N*-Methyl pyrrolidone and DI mixture
 104 solution;

105 (b) The salts (e.g., copper sulfate was used for copper plating, and nickel sulfate for nickel
 106 plating), reducing agents (e.g., ascorbic acid in the copper plating and sodium borohydride in the
 107 nickel plating) and surfactant agents were mixed together to form an electroless plating solution
 108 (Figure 1(b));

109 (c) Then the GO suspension solution was added into the electroless plating solution (Figure
 110 1(c));

111 (d) The mixed solution was intensively stirred using a magnetic stirrer to disperse the GO
 112 suspension solution. The copper plating process was done at 90 °C for 3 hours, and the nickel
 113 plating was done at 30 °C for 30 min. Simultaneously the NaOH solution or ammonia solution was
 114 dripped into the mixed solution to adjust the pH value to between 9 to 10 (Figure 1(d)). The pH
 115 value in the bath was continuously measured using a pH meter, and was maintained by adjusting
 116 the added NaOH solution or ammonia solution using a peristaltic pump. The temperature during
 117 the electroless plating process was controlled using a fixed-temperature water bath.

118 (e) The precipitates were separated from the solution after the chemical reactions were
 119 completed (Figure 1(e)). DI water and ethanol solution were used to wash the precipitates for
 120 several times, and dried at 60 °C for 8 hours using a vacuum freeze-drying method.



121

122 **Figure 1.** Illustration of the preparation process of Cu@graphene powders and Ni@graphene: (a)
 123 dispersion of oxidized graphite in dispersing agent; (b) electroless plating solution; (c) adding GO
 124 suspension solution to electroless plating solution and stirred; (d) mixture solution was stirred at
 125 the same time with dripped NaOH or NH₃·H₂O; (e) precipitates were filtrated, cleaned and freeze
 126 drying.

127 2.4. Characterization

128 An X-ray diffractometer (XRD-7000S, Shimadzu, Japan) with Cu K_α radiation at 40 kV and 15
 129 mA was used to analyze the crystalline structures of GO and metal@graphene. The scanning rate
 130 was 8 °/min and the scanning range of 2θ was 5 ~ 65° with a step size of 0.02°. Surface morphology
 131 of the GO and metal@graphene was observed using a scanning electron microscope (SEM, TESCAN
 132 VEGA3 XMU) and chemical element analysis was performed using an energy dispersive X-ray
 133 spectrometer (EDS). Detailed morphological characteristics of the GO and metal@graphene
 134 composites were obtained using a transmission electron microscope (TEM, JEM-3010).
 135 Characterization of samples using Raman spectroscopy (Renishaw, Via Reflex) were performed
 136 using a laser beam with a wavelength of 532 nm and a SWIFT detector over a range of 500-3500 cm⁻¹,
 137 and all the spectra were taken at room temperature (20 °C). Fourier transform infrared (FT-IR)
 138 spectra of the GO and metal@graphene were obtained using a TENSOR 27 spectrophotometer
 139 (Bruker, Germany) with wavelengths ranging from 500-4000 cm⁻¹ at room temperature. Microscale
 140 surface morphologies of metal@graphene powders were obtained using an atomic force microscope
 141 (AFM, FM-Nanoview6800) in a tapping mode.

142

143 2.5 Modeling and calculation details

144 For the graphene system after atomic adsorption, there are defects, grain boundary and
145 intrinsic atoms formed. The adsorption energy of defects on the graphene is maximum, and those of
146 the grain boundary and intrinsic atoms on the graphene are approximately equal. The binding
147 between graphene and metal is generally weaker than a typical covalent bond. In the present study,
148 we focused on analysis of cohesive energies of copper and nickel atoms with both their (111)
149 surfaces bonded onto a graphene of a few atomic layers. The modeling work only considered the
150 intrinsic atoms and defects adsorption. The first principle calculation was used to evaluate the
151 cohesive energy between graphene and metal interface, as the binding force cannot be obtained
152 using experimental methods easily.

153 The interface between graphene and copper (or nickel) was modeled using a supercell, whose
154 lattice constant was set as $a=b=2.46$, $c=3.4$, with the added carbon atoms set as $a=0.333$, $b=0.667$, and
155 $c=0.5$. The vacuum layer was applied with 2 nm above on the c -axis direction in order to eliminate
156 the influence of graphene layers. Finally, a and b values in the supercell were expanded to three
157 times of their original ones, and the initial configuration of the model was maintained?? (as shown
158 in Figure S1). The structures and properties of the composite system were investigated based on the
159 density functional theory (DFT) using the Vienna Ab-initio Simulation Package (VASP) software
160 and the DMol3 quantization package [29,30], the latter of which is a module in the Materials Studio
161 package, and stands for the basic vector using the numerical value of the atomic orbitals. The
162 self-consistent solution of the DFT equation was acquired by numerical integrations in order to
163 obtain the electron property, wave function and charge distribution of the composite system.
164 During the calculation, the settings were verified in order to achieve a total energy convergence less
165 than 500 eV. For the geometry relaxation, the force applied onto atoms was converged below a
166 threshold of 0.001 eV. For the Brillouin zone integration, Monkhorst–Pack sampling k -points of 4×4
167 $\times 1$ were chosen in this study.

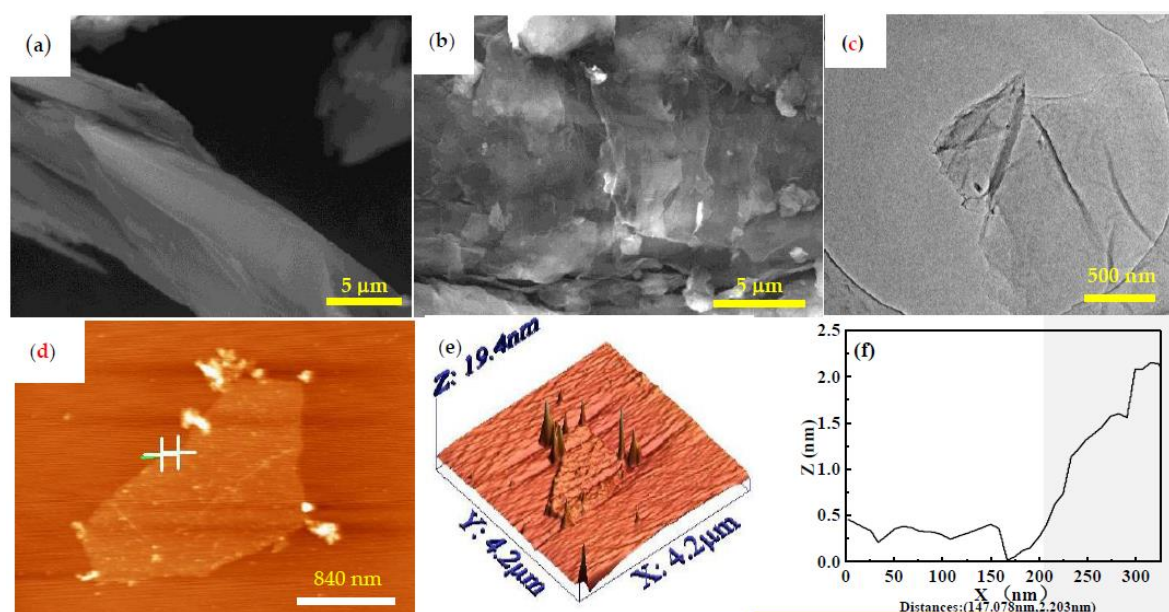
168 3. Results and discussions

169 3.1. Microstructure characterization and morphology analysis

170 Figures 2(a) and 2(b) show SEM images of the flakes of graphite and GO. The graphite (Figure
171 2(a)) shows large sizes of flakes, and its surface is smooth and flat. Whereas the surface of GO
172 (Figure 2(b)) has many ripples, folds and bumps, and is quite rough with apparent lamellar
173 structures. The edges of the GO sheets have apparent folding structures. Comparison of the images
174 in Figures 2(a) and 2(b) reveals that after the graphite was oxidized, the flat surface of the graphite
175 disappears due to the oxidation process. There are various structural defects such as mosaic,
176 vacancies and impurity atoms in the crystalline structure of graphite [31].

177 In order to check the thickness and microstructure of the GO, TEM and AFM images were
178 obtained and the results are shown in Figures 2(c)~2(f). GO shows a crumpled sheet structure
179 (Figure 2(c)). As can be seen from Figures 2(d) and 2 (e), the thickness of the GO sheet is about 2.203
180 nm. It was reported that the thickness of a monolayer GO was about 1.2 nm [32]. The thickness of
181 the GO sheet in this study is thicker, which could be explained by the fact that the oxidized
182 graphene sheets are bonded with hydroxyl and epoxy groups from both sides. Besides, the surface
183 wrinkles and the presence of water molecules on the surface of the GO could also increase the
184 measured thickness of the GO sheet from the AFM test [32]. The thickness of GO measured in this

185 experiment was 2.203 nm, thus the thickness of GO could be about 2 to 3 layers.



186
187 **Figure 2.** SEM images of (a) Flake graphite and (b) GO, (c) TEM and (d) AFM images of GO, (e) 3D image of
188 surface image, (f) cross-section analysis of the height of graphene using AFM.

189 AFM and TEM images of graphene, Cu-coated graphene and Ni-coated graphene obtained
190 from the *in-situ* co-reduction processes are shown in Figure 3. As shown in Figure 3(a), the
191 graphene is transparent with wrinkled structures. Comparing Figure 3(b) with 3(d), the Cu or Ni
192 particles were coated on the surface of graphene which forms the loose and porous surfaces [33],
193 suggesting that the thickness of the graphene after coated with the copper or nickel particle would
194 be increased.

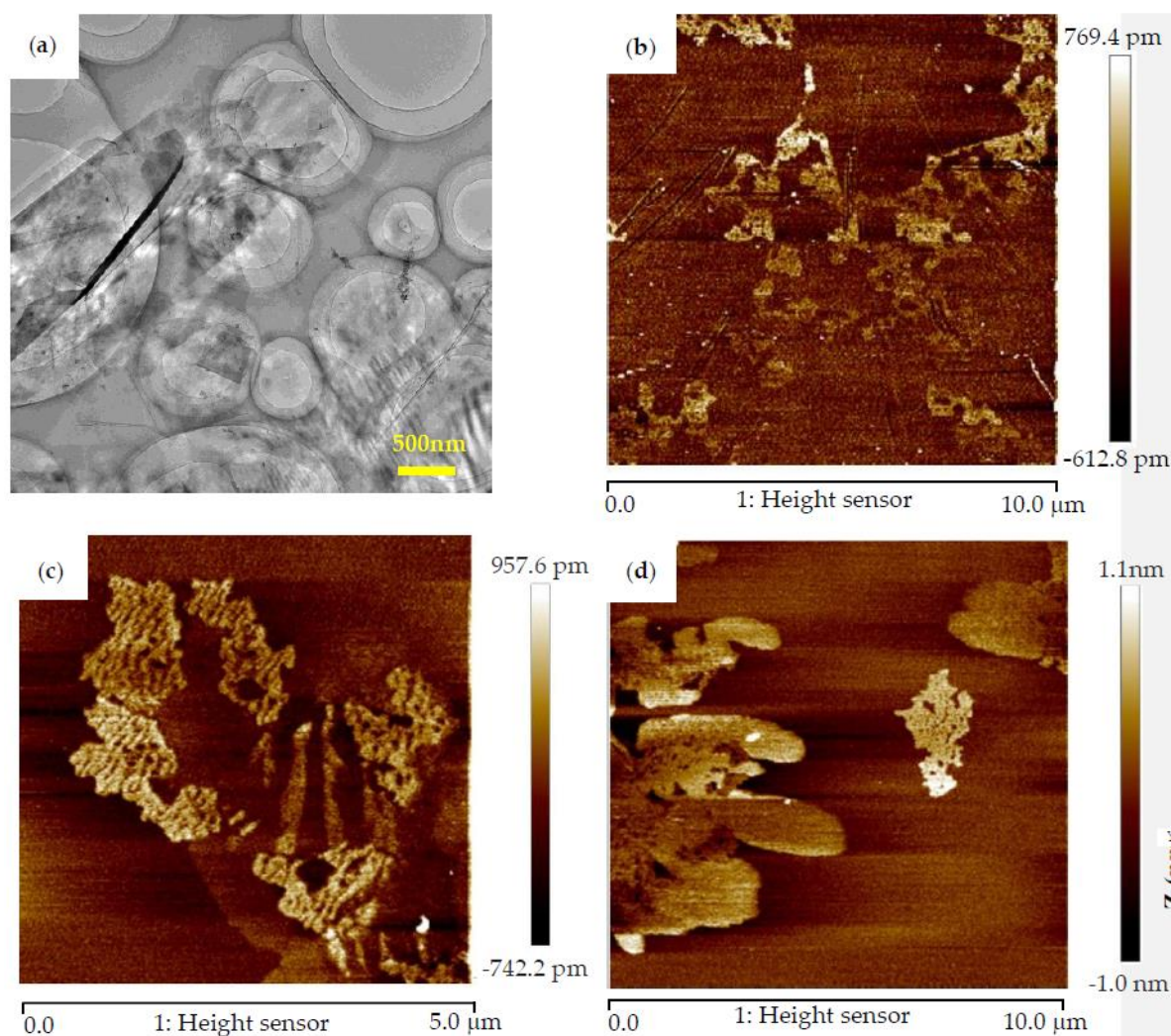
195 The obtained XRD patterns of GO sheets, graphene, Cu@graphene sheets and Ni@graphene
196 sheets are shown in Figure 4. For the GO (Figure 4(a)), a sharp peak was observed near the
197 diffraction angle 2θ of 10° , which is the characteristic peak of the GO [24]. This shows that the
198 graphite has been successfully oxidized into GO through the intercalation process. Generally, the
199 spacing of GO inter-planar spacing can be estimated using the Bragg Equation (1):

$$2d\sin\theta = n\lambda \quad (1)$$

200 where n is 1, λ is the X-ray wavelength of 0.154 nm from the Cu X-ray source, θ is half of the
201 diffraction angle, and d is the interlayer spacing. The calculated layer spacing of peak (001) of
202 graphite oxide is ~ 0.80 nm, which indicates that the GO obtained is nearly a monolayer [34].

203 For XRD result of Cu@graphene (Figure 4(c)), there are three dominant diffraction peaks at
204 43.3° , 50.4° and 74.1° , respectively, corresponding to three face-centered cubic copper crystal (111),
205 (200), and (220). The characteristic peak corresponding to the (002) crystal plane of graphene was
206 found to be at $2\theta = 26^\circ$, and it is relatively weak when compared to the copper peaks [27]. The peaks
207 of cuprous oxide were also found in the XRD pattern of Cu@graphene sheet, indicating that some
208 cuprous oxides were formed during the chemical reaction process.

209



210
211
212

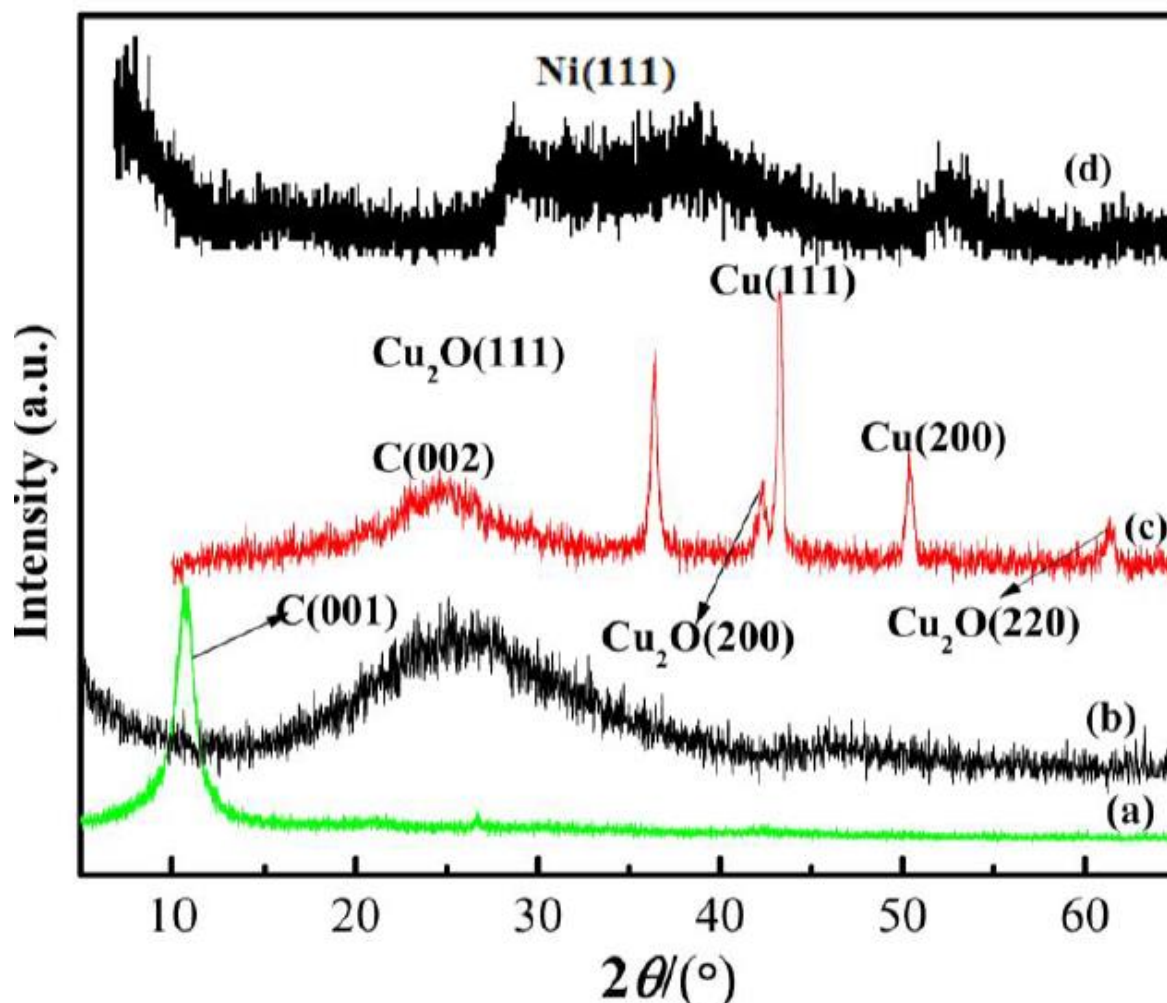
Figure 3. (a) TEM of graphene and AFM images of (b) graphene, (c) Cu-decorated graphene and (d) Ni-decorated graphene

213 For XRD result of the Ni@graphene sheets (Figure 4 (d)), there is a broad peak at $2\theta = 44.5^\circ$
214 which is corresponding to the (111) plane of nickel, indicating that the crystallinity of nickel on the
215 surface of graphene is relatively poor and the nickel on the surface of graphene may be in a
216 amorphous or nano-crystalline structure. However, there is no obvious peak observed near the
217 diffraction angle 2θ of 26.3° , which is because the surface of graphene sheets is covered with Ni
218 metal layer.

219 In order to verify that the graphene was still maintained after the *in-situ* co-reduction process,
220 XRD analysis of the prepared composites (Figure 4(b)) shows a broad diffraction peak at 22.5° .
221 Comparing Figure 4(c) with Figure 4(d), it can be seen that the diffraction peak of the composite is
222 similar to the graphene, instead of GO [35].

223 Raman spectra of GO, graphene, Cu@graphene and Ni@graphene powders are presented in
224 Figure 5. The Raman spectrum of the GO in Figure 5(a) exhibits three characteristic peaks at 1349.09,
225 1593.06 and 2700 cm^{-1} , which represent the D peak, G peak and 2D peak of the GO. The intensity
226 ratio of D peak and G peak (I_D/I_G) is often used to characterize the degree of defects in carbon
227 materials [21]. The I_D/I_G of GO in this study was measured to be 0.91, and it is similar to those
228 reported in references [36, 37].

229



230

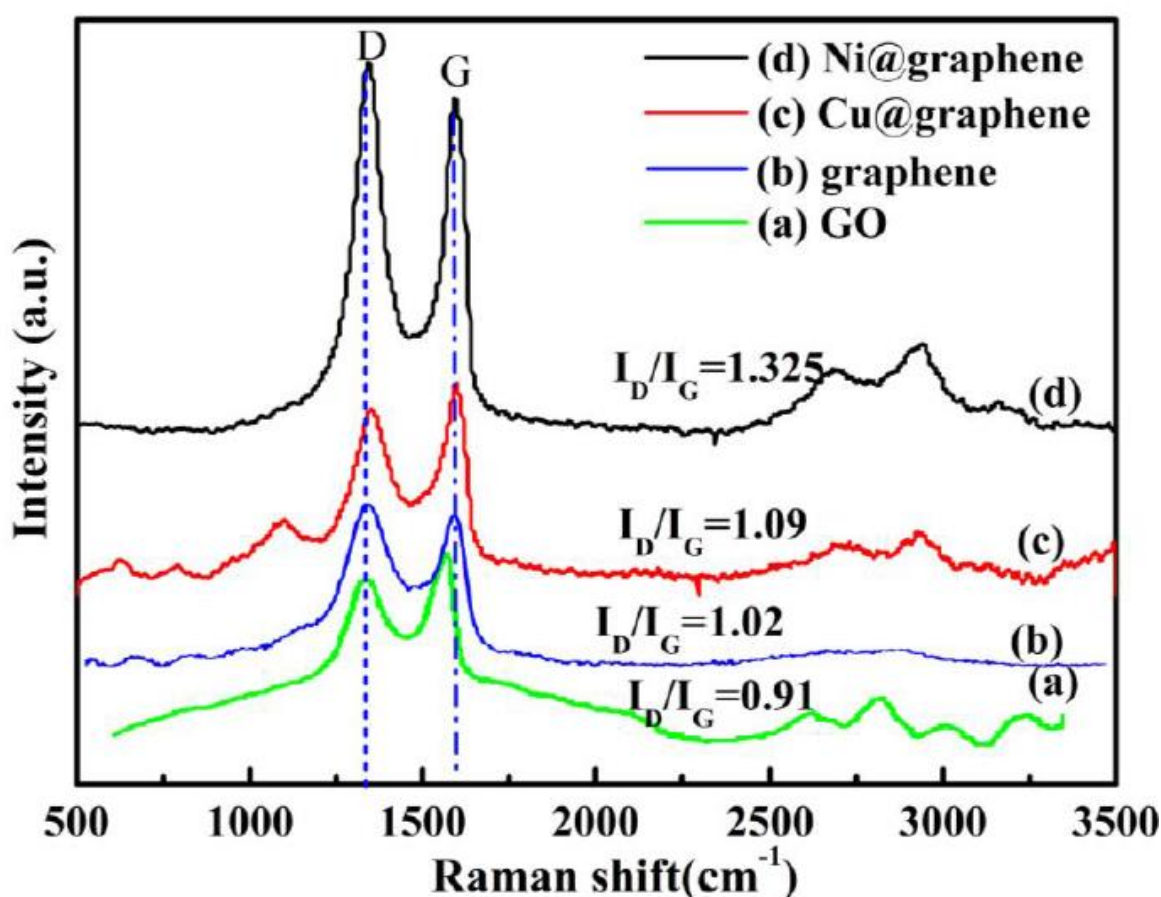
231

Figure 4. XRD patterns of (a) GO, (b) Graphene, (c) Cu@graphene and (d) Ni@graphene

232 Comparing the I_D/I_G data of composites and graphite, we can confirm that the defects are
 233 increased after the graphite was oxidized and some of the carbon atoms in the defect structures are
 234 combined with the oxygen-containing functional groups [38]. Formation of these highly active sites
 235 of defects can promote the adsorption of metal ions in the subsequent plating process. After the
 236 graphite is oxidized, some of the carbon atoms in the structure are combined with the
 237 oxygen-containing functional groups and transform from sp^2 hybridization into sp^3 hybridization.
 238 The oxygen-containing functional groups not only cause changes in crystallinity of hexagonal
 239 network structures of the graphite, but also increase the defects, which causes the G peak to be
 240 widened and the strength of D peak to be increased [39]. Whereas for graphene, the ratio of I_D/I_G is
 241 1.02 as shown in Figure 5(b). Therefore, the increased ratio of I_D/I_G for the composite indicates that
 242 majority of oxygen-containing functional groups were removed during the reduction process, the
 243 reason of which has been reported in our previous work [40, 41].

244 Raman spectrum (Figure 5(c)) of the Cu@graphene composite exhibits two characteristic peaks:
 245 i.e., $\sim 1352.07\text{ cm}^{-1}$ and $\sim 1593.06\text{ cm}^{-1}$, which represent the D peak and G peak of carbon. The
 246 calculated I_D/I_G values of GO and Cu@graphene are 0.91 and 1.09, respectively. This indicates that
 247 the reduction effect will result in the increases of defects, topological disorders and the degree of
 248 graphitization; as well as decrease of crystallinity. The Raman spectrum of the Ni@graphene

249 composite (Figure 5(d)) has two prominent peaks corresponding to $\sim 1340.17 \text{ cm}^{-1}$ of the D peak and
 250 $\sim 1593.06 \text{ cm}^{-1}$ of the G peak. It can be seen that the I_D/I_G of Ni@graphene is 1.325, which is much
 251 larger than the value of 0.91 for the GO. This shows that after the surface of graphene is coated with
 252 nickel, the crystallinity is decreased and the defects are increased. This also shows that after the GO
 253 has been reduced into graphene, the oxygen-containing functional groups are decreased on the
 254 surface of GO [42]. Therefore, the π bond has been recovered and the defects and disorder are
 255 increased.



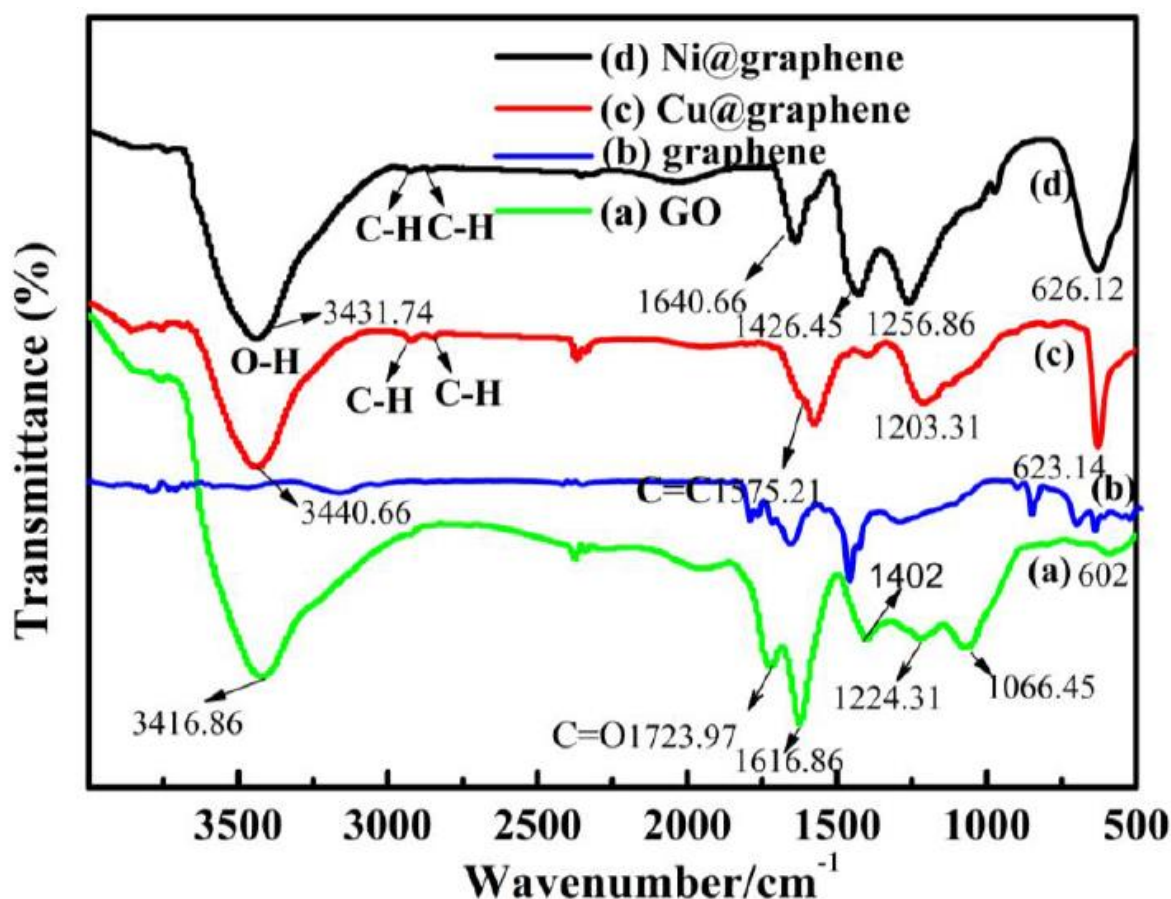
256
257

Figure 5. Raman spectra of (a) GO, (b) graphene, (c) Cu@graphene and (d) Ni@graphene

258 The Raman 2D peak (2711.88 cm^{-1}) is originated from two phonon and double resonances of
 259 laser induced vibration process for carbon. Generally, the 2D peak is an indication if the graphene is
 260 single layer or a few layers [43]. Previous studies showed that the 2D peak was shifted to the
 261 direction of large wave-number side as the number of graphene layers was increased [36]. The
 262 unique 2D peak of the single-layer graphene is located at 2678.8 cm^{-1} , whereas that of double-layer
 263 graphene is located at 2692.3 cm^{-1} , and that of graphene having more than 10 layers is close to the
 264 position of the 2D peak of natural graphite which is located at 2716.5 cm^{-1} . The 2D peak of GO in
 265 this study (Figure 5(a)) is located at 2700 cm^{-1} , indicating the GO has a few layers [38]. The 2D peak
 266 of the Cu@graphene (Figure 5(c)) is located at 2706 cm^{-1} , which indicates the layer of graphene is
 267 between two and ten. The 2D peak of the Ni@graphene (Figure 5(d)) is located at 2680 cm^{-1} , which
 268 shows that the nickel-plated graphene has one monolayer. It also suggests that the graphene layer
 269 became thinner when the sodium borohydride was used as the reducing agent. This indicate that
 270 the graphene layer was slightly thicker when the ascorbic acid was used as the reducing agent.

271 Figure 6 shows the FT-IR spectra of the prepared samples. The FT-IR spectrum of the GO sheets

272 in Figure 6(a) shows many peaks: e.g., absorption peaks due to the -O-H stretching vibration of
 273 hydroxyl groups; water in the GO at 3416.86 cm^{-1} ; the -C=O stretching mode at 1723.97 cm^{-1} ; the
 274 vibration mode of -O-H at 1402 cm^{-1} ; the -C-OH stretching vibration at 1066.45 cm^{-1} ; and the
 275 absorption peak at 1616.86 cm^{-1} [44]. Based on the appearance of oxygen functional groups on the
 276 surface of GO measured by the FT-IR and the changes in the morphology of GO from the SEM
 277 observation, we can conclude that graphite has been intercalated into GO sheets. In general, the
 278 FT-IR spectrum of graphene is quite similar to that of GO [18]. However, the intensities of all the
 279 peaks correlated to the oxygen functional groups of graphene are decreased dramatically if
 280 comparing Figure 6(a) with Figure 6(b).



281

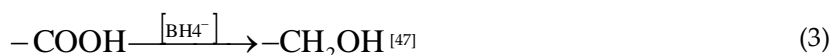
282

Figure 6. The FT-IR spectra of (a) GO, (b) graphene, (c) Cu@graphene and (d) Ni@graphene

283 Comparing the FT-IR spectra of GO and Cu@graphene (Figure 6(c)), it can be seen that the
 284 absorption peaks of both hydroxyl group and carboxyl group are decreased after the plating
 285 process, mainly due to the deposition of the copper particles and reduction of GO. The -C=O
 286 stretching vibration peak at 1723.97 cm^{-1} disappears for the Cu@graphene sample. Results show that
 287 after the GO is reduced, the conjugated structure is restored. The FT-IR spectrum of the graphene
 288 (Figure 6(c)) is smoother than that of the GO (Figure 6(a)), indicating that the functional groups on
 289 the surface of graphene are much less than those on the surface of GO (Figure 6(a)). Also the
 290 oxygen-containing functional groups on the surface of the GO are decreased [45].

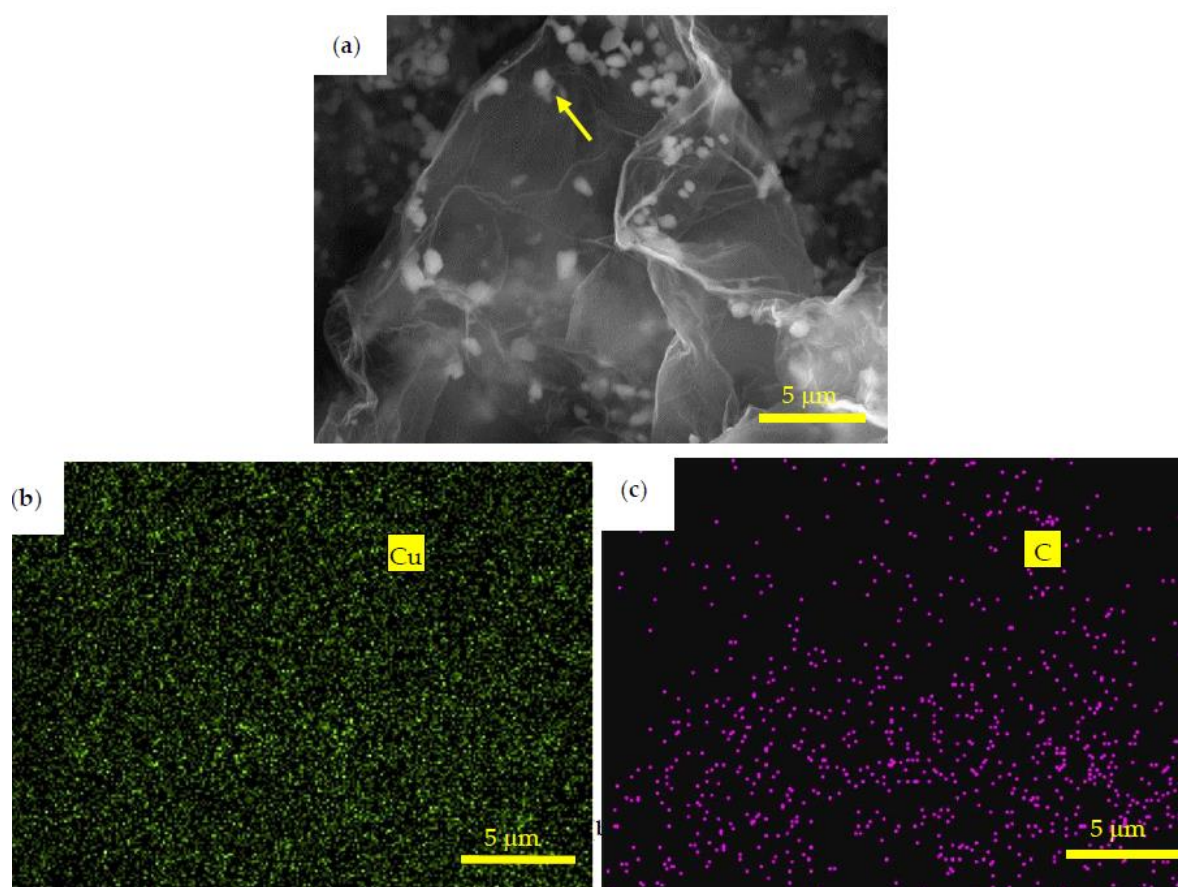
291 For the FT-IR spectrum of the Ni@graphene (Figure 6(d)), all the characteristic peaks in the
 292 FT-IR spectra of GO are weakened due to the deposition of nickel particles onto the surfaces of
 293 graphene sheets. The -C=O stretching peak at 1723.97 cm^{-1} disappears, but there are -C-H
 294 anti-symmetrical stretching vibration peak at 2922.98 cm^{-1} and -C-H symmetrical stretching

295 vibration peak at 2851.57 cm^{-1} , indicating that the $-\text{COOH}$ groups on the surfaces of the GO sheets
 296 were reduced into $-\text{CH}_2\text{OH}$ by using the NaBH_4 . This phenomenon shows that there are new
 297 chemical bonds generated between nickel particles and graphene, not just a simple physical
 298 adsorption. This chemical bond formations from the reactions can be written using Equations
 299 (2)-(3):



300 Figure 7(a) is a back-scattered electron (BSE) image of Cu@graphene synthesized using the
 301 *in-situ* co-reduction method. The white nanoparticles are uniformly dispersed in a semi-transparent
 302 and folded graphene substrate and no obvious aggregation is observed. The white fine particles are
 303 copper based on the EDX analysis. The images of EDX elemental mapping of the Cu@graphene
 304 after the reduction process are shown in Figures 7 (b) ~ 7(c). Results show that there are elements of
 305 C and Cu which are uniformly distributed in the Cu@graphene. The copper particles coated on the
 306 graphene tend to be deposited onto the edges and folds of graphene sheets. This is consistent with
 307 the reported distribution of copper particles on the surface of graphene in the Cu@graphene in the
 308 literature [46].

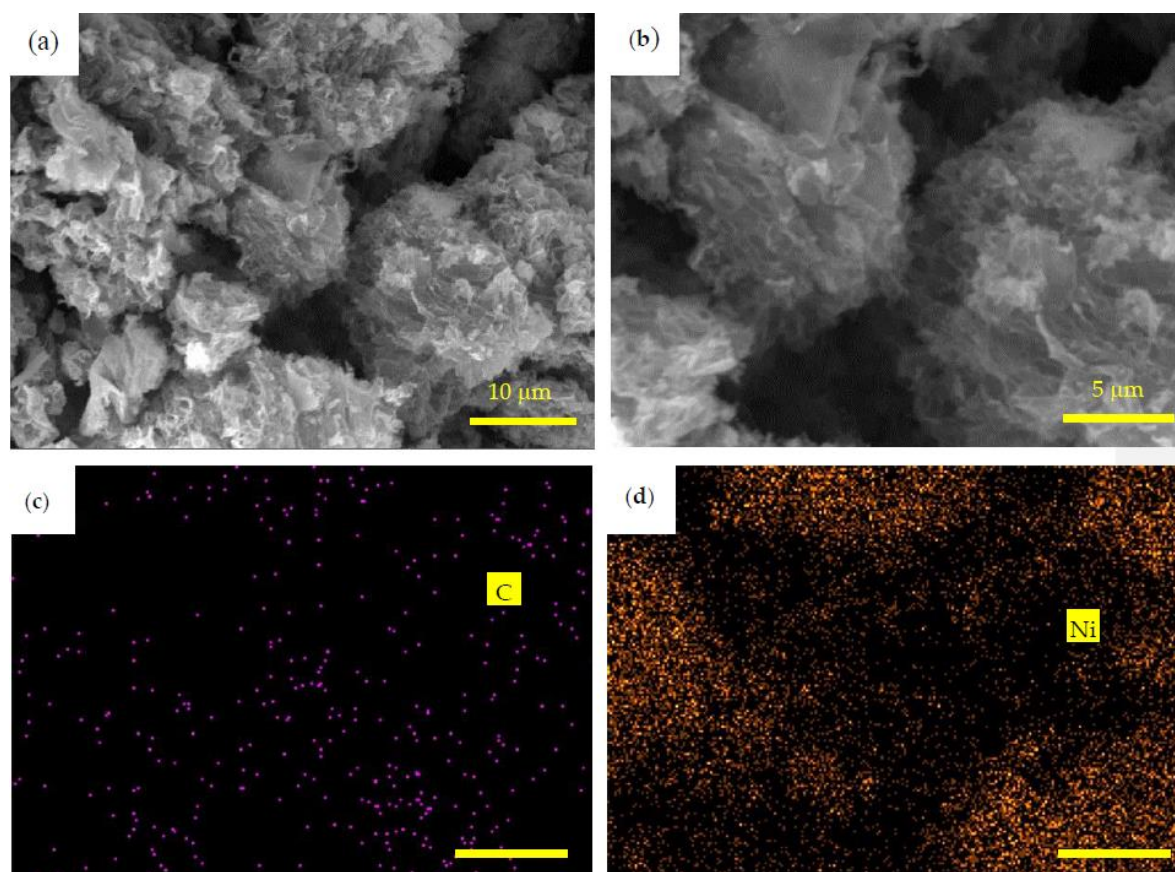
309
 310



311
 312
 313

Figure 7. (a) Backscattered electron image and (b) to (c) EDX Cu element mapping and C element mapping of Cu@graphene

314 Figure 8(a) is a BSE image of Ni@graphene. It can be seen that the graphene is made up of a
315 wrinkled and folded membrane. From Figure 8(b), the graphene sheets are stacked and
316 agglomerated, probably due to the fact that the monolayer nickel-coated graphene sheets are not
317 completely dried before bonded with the graphene layer, which has also been reported in the
318 literature [16]. EDS elemental mapping of the Ni@graphene is shown in Figures 8(c) ~ (d). Results
319 showed that there are elements of C and Ni uniformly distributed in the graphene.

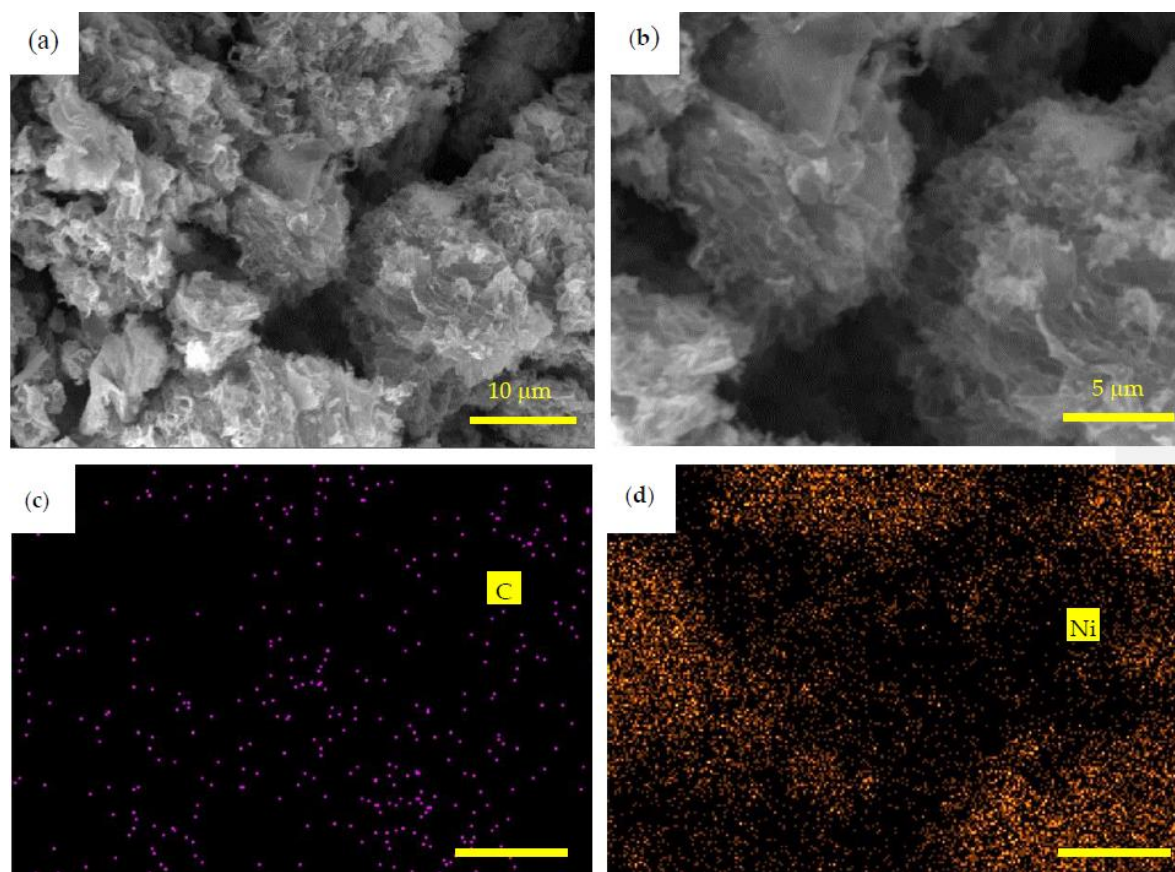


320
321
322

Figure 8. (a) and (b) Backscattered electron image and (c) to (d) EDX C element mapping and Ni element mapping of Ni@graphene

323 TEM images of GO and Cu@graphene are shown in Figure 9. The GO sheets were exfoliated
324 into thin layers, and its specific surface areas are quite large as shown in Figure 9(a). Formation of
325 large two-dimensional planes of the reduced GO results in a uniform deposition of copper on its
326 surface. At the same time, oxygen-containing functional groups on the surface and edges of GO can
327 react with copper ions, which lead to the uniform distribution of copper on the GO surfaces during
328 plating process. Figure 9(b) shows that there are black particles with diameters of ~200 nm
329 distributed in the substrate background. Selected area diffraction (SAED) patterns (Figure 9(c))
330 confirm that the black area is copper and the gray background area is graphene. Graphene exhibits
331 a yarn-like and translucent layered structure, and its surface is not perfectly flat but with a wrinkled
332 and folded sheet-like morphology. This is because the graphene is a two-dimensional material, and
333 folds and ripples are easily generated in order to maintain its thermodynamic stability [8]. This is
334 consistent with the microscopic morphologies of graphene reported in the literature [24, 48]. The
335 copper particles on the surface of graphene are mainly distributed in the folds and marginal areas
336 of the graphene, which is consistent with what has been reported in the literature [22]. This is
337 mainly due to the larger energy and higher catalytic activity of the folds and marginal areas, which

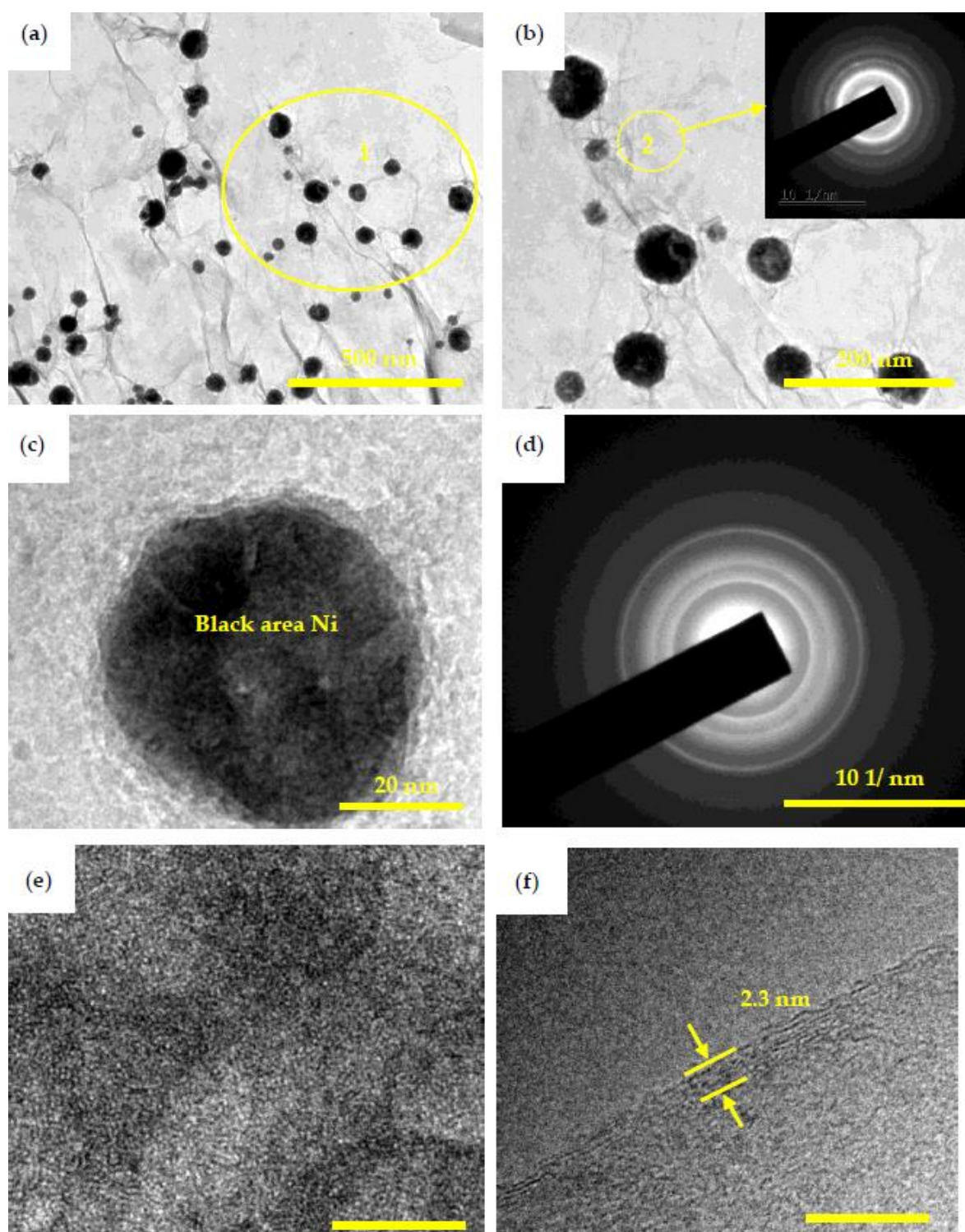
338 enhances the easier deposition of metal particles. Distinct lattice fringes of Cu can be observed in
339 the HRTEM image as shown in Figure 9(d). The lattice parameter was measured to be 0.21125 nm,
340 corresponding to the interplanar spacing of Cu (111) plane. This indicates the successful obtaining
341 of Cu@graphene, similar to those reported in the literature [46]. These results are also consistent
342 with those from the XRD and SEM.
343



344 **Figure 9.** TEM images of Cu@graphene (a) original GO (b) Cu@graphene after reduced by ascorbic
345 acid; (c) single Cu particle on graphene; Insets are the corresponding SAED patterns; (d) HRTEM
346 of Cu particle on graphene
347

348 TEM image of the Ni@graphene is shown in Figure 10(a). The SAED pattern taken from the
349 enlarged area of Ni@graphene (Figure 10(b)) indicates that there are several concentric halo patterns.
350 The boundary of each halo is not clear, which confirms that the gray area is a signal of amorphous
351 carbon, it could be caused by the defects of graphene during the reduction. Figure 10(c) shows a
352 single Ni particle whose size is around 55 nm, and the Ni particle is semi-amorphous or
353 nano-crystalline, as illustrated by the SAED pattern (Figure 10(d)). This is consistent with XRD
354 results and also those reported in the literature [49,50]. The electroless nickel plating generally
355 produced an amorphous structure, and post-annealing was needed for its subsequent conversion
356 into crystalline structures (generally at 701-719 K) [48, 51-53]. The crystalline structures of Ni
357 deposited on the surface of graphene were reported to be influenced by the post-treatment
358 temperature after plating. When the temperature is less than 473.15 K, the nickel is amorphous;
359 whereas it is crystallized when the temperature is higher than 573.15 K. Nickel oxide can be formed
360 at much higher temperatures [44]. The post-treatment temperature used in this study was 333.15 K,

361 lower than previously reported. Therefore, this is the main reason for widening



362

363 **Figure 10.** TEM images of Ni@graphene (a) and (b) TEM picture of Ni@graphene after
 364 reduced by sodium ascorbate; Insets are the corresponding SAED patterns;(c)single Ni
 365 particle on graphene; (d)the electron diffraction pattern of (c); (e)HRTEM of Ni particle
 366 on graphene; (f) HRTEM of graphene

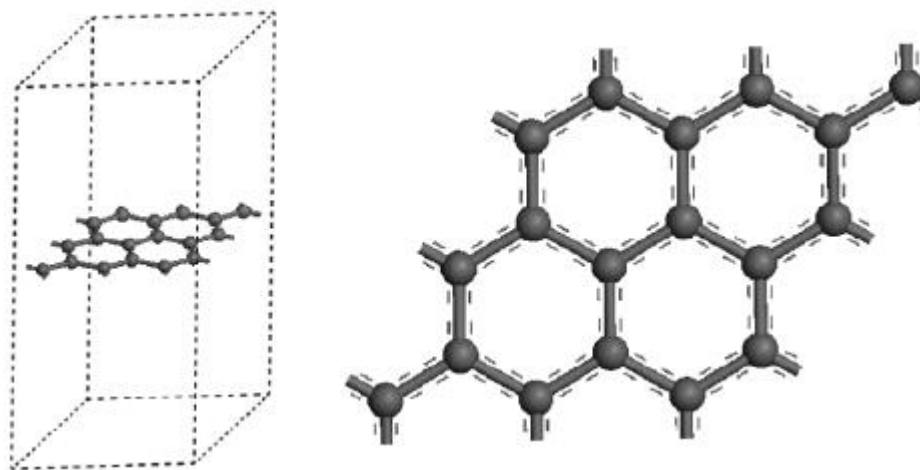
367 of the SAED diffraction peak or poor crystallinity of Ni, which is consistent with the
 368 result of XRD analysis. The crystal structures of nickel deposited on the surface of

369 graphene may also be affected by the synthesis methods. For example, nickel/graphene
370 prepared using a chemical vapor deposition method produced a crystal structure, [24]
371 and Ni-nanoparticles/graphene composite fabricated using a solvothermal method also
372 showed a crystalline structure [17]. The HRTEM of the single Ni particle is shown in
373 Figure 10 (e). Clearly the crystallinity of the deposited nickel is not good, consistent with
374 the results obtained from both electron diffraction and XRD analysis. The distribution of
375 nickel particles (Figure 10(a)) mainly exists in the edges and folded areas of graphene,
376 similar to those reported in literature [54]. Also, the HRTEM of graphene is shown in
377 Figure 10(f), and graphene of ~ 6 atomic layers can be clearly observed, with a thickness
378 of 2.3 nm, as denoted by the yellow arrow in Figure 10(f). Clearly a few layers of
379 graphene in Ni@graphene can be formed using our proposed method, which further
380 confirms the AFM result and analysis.

381 3.2. Cohesive interfacial energy analysis between graphene and metal using first-principle calculations

382 Based on DFT calculation results, the binding energy of Ni atoms adsorbed onto the graphene
383 is 2.078 eV, whereas the binding energy of Ni atoms adsorbed on the graphene with the defect is
384 3.214 eV. Meanwhile, the binding energy of Cu atoms adsorbed onto the intrinsic graphene is 1.778
385 eV, whereas that of Cu atoms adsorbed on the graphene with the defect is 5.114 eV. For both cases,
386 the binding of metal atom and graphene is a chemical process, which verifies the experimental
387 results in the previous sections. Meanwhile, results show that the binding energy of atomic
388 adsorption on defect of graphene is larger than that on the intrinsic graphene, which clearly show
389 that the metal atoms are preferably adsorbed on the defects in the graphene. This result is also
390 consistent with the literature [55,56].

391 In order to know the differences of binding strengths between copper or nickel and graphene,
392 we further analyzed the electronic coupling across the interfaces. The obtained band structures of
393 graphene–Cu(111) system and graphene–Ni(111) system are plotted in Figure 11. The results show
394 that the Fermi level is pinned to the Cu or Ni bands, i.e. electrons are transferred from π bands in
395 the graphene layer onto metal bands. The coupling between the orbital of carbon atoms and the
396 orbital of metal atoms is weak, and electrons in the metal bands are transferred into the graphene
397 layer. Consequently, the Fermi level is close to the boundary between conjugated π bands of the
398 graphene. The coupling between the Pz orbital of carbon atoms and the metal atoms is strong.
399 Therefore we find that, except for the observed charge transfer between graphene and metal orbitals,
400 a strong coupling is obtained between the band structures of graphene and metal.



Figure

401

402 **11.** Electronic band structures of (a) graphene–Ni and (b) graphene–Cu composite systems

403 3.3. Formation mechanisms of metal@graphene

404 Based on the characterization results, the formation mechanism of metal@graphene is proposed
 405 as illustrated in Figure 12. Our *in-situ* co-reduction method for fabrication of Cu@graphene or
 406 Ni@graphene composites starts from the selection of the appropriate salts which can provide
 407 suitable metal ions according to the plated metal (i.e., copper sulfate was used for copper plating).
 408 Anions of the oxygen-containing functional groups at the edges and surfaces of the GO attract
 409 copper ions or nickel ions in the plating solution, therefore, a large amount of copper ions or nickel
 410 ions are adsorbed on the surfaces and edges of the GO.

411 In the second stage, a suitable chemical reagent and a strong reducing agent (i.e., ascorbic acid
 412 in the copper plating and sodium borohydride in the nickel plating) are applied depending on the
 413 type of metal to be plated and the chemical reduction processes to be initiated.

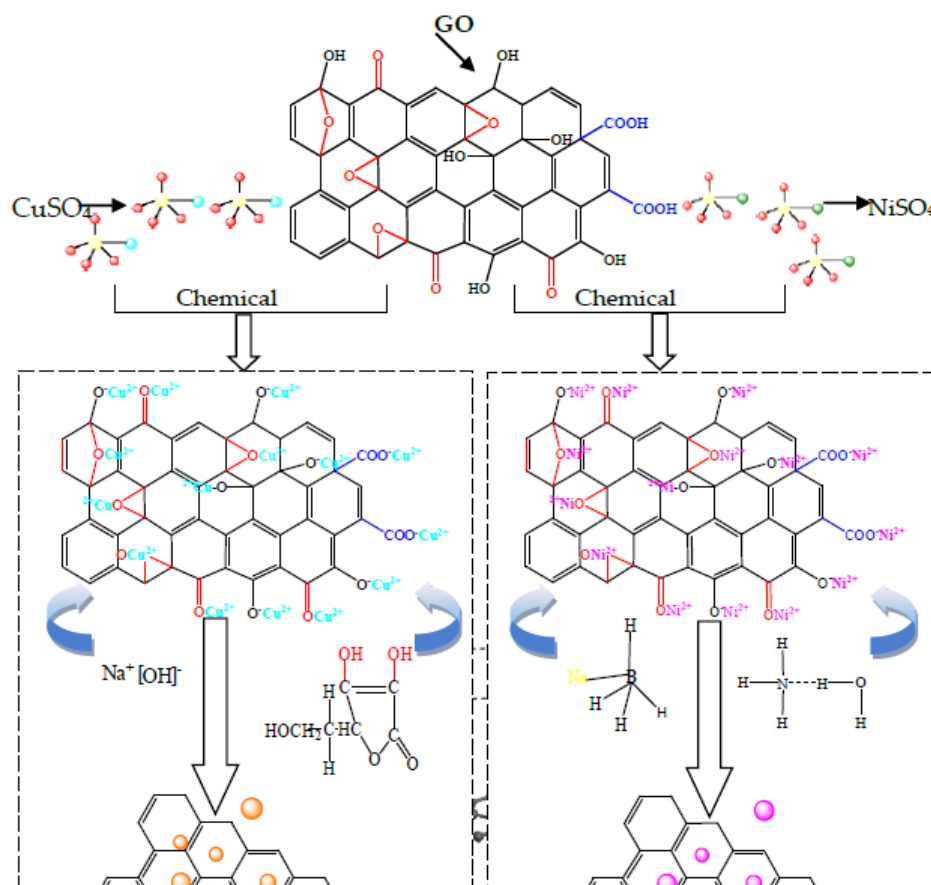
414 The third step is the most important one which is *in-situ* and co-reaction process. The copper
 415 ions or nickel ions adsorbed on the edge and surfaces of graphene oxide are strongly reduced in the
 416 alkaline conditions to obtain metal particles, and the specific reactions for copper plating are written
 417 in Equations (4)–(7). Those of the nickel plating are written in Equation (8):



418 Simultaneously, GO is reduced by the strong reducing agent of ascorbic acid or sodium
 419 borohydride to produce a graphene layer. The –COOH functional group on the surface of the GO is
 420 reduced to –CH₂OH with the reduction actions of ascorbic acid or sodium borohydride. The
 421 reduction reactions can be verified from our FT-IR analysis. The reactions that occur in this process
 422 can be expressed as follows:



423 Since the newly formed graphene has a large surface energy, the metal ions in the solution are
 424 easily adsorbed onto the surface of the graphene and then deposited onto its surface, and the
 425 inherent "defects" of the graphene cause the metal ions to form a good chemical bonding [57]. This
 426 has been verified by both the Infrared and Raman analysis results.



427

428 **Figure 12.** Schematic illustration of reaction mechanism of Cu@graphene and Ni@graphene

429 4. Conclusion

430 In this work, GO of 2~3 atomic layers were obtained using the Hummer's method. Using GO,
 431 copper sulfate and ascorbic acids (or nickel sulfate and sodium borohydride), the Cu@graphene
 432 powders (or Ni@graphene powders) with a homogeneous distribution of metal nanoparticles on the
 433 surface of graphene were obtained using an efficient *in-situ* co-reduction method. The formation
 434 mechanism of metal@graphene can be explained: e.g., the metal ions and graphene firstly form a
 435 chemical bond, and the GO and the metal ions are simultaneously reduced by the reducing agents
 436 to finally obtain the metal@graphene. The binding of metal atom and graphene is a chemical
 437 process which can be verified based on the results from the first-principle calculations.

438 **Author Contributions:** Wenge Chen supported and assisted in supervision on the project; Longlong Dong
 439 planned and supervised the project; Yongqing Fu supported and advised on the project; Jiaojiao Wang, Yuanlin
 440 Xue and Qian Zhao designed and performed the experiments; Jiaojiao Wang made the microstructure
 441 characterization and phase structure. Jiaojiao Wang, Wenge Chen, Yuanlin Xue analyzed data and wrote the
 442 manuscript, and all the authors modified and corrected the manuscript.

443 **Acknowledgements:** The authors would like to acknowledge the financial support from Key Research and
444 Development Projects of Shaanxi Province (No. 2017ZDXM-GY-050) and Electrical Materials and Infiltration
445 Key Laboratory of Shaanxi Province Projects (No. 17JS080), Xi'an Science research project of China (No.
446 2017080CG/RC043), the National Security Major Basic Research Plan of China and the Northwest Institute for
447 Nonferrous Metal Research (K1652-1, K1652-12, K1740), Newton Mobility Grant (IE161019) through Royal
448 Society and the National Natural Science Foundation of China, and Royal academy of Engineering
449 UK-Research Exchange with China and India.

450 References

- 451 1. Lee, C.J.; Wei, X.D.; Kysar, J.W.; Hone, J. Measurement of the elastic properties and intrinsic
452 strength of monolayer graphene. *Science* **2008**, *321*, 385-387.
- 453 2. Pham, K.D.; Hieu, N.N.; Ilyasov, V. V.; Phuc, H.V.; Hoi, B.D.; Feddig, E.; Thuanh, N. V.; Chuong
454 V. N. First principles study on the electronic properties and Schottky barrier of Graphene/InSe
455 heterostructure. *Superlattices and Microstructures* **2018**, *122*, 570-576.
- 456 3. Khalil, K.; Kambiz, Vafai Analysis of the anomalies in graphene thermal properties.
457 *International Journal of Heat and Mass Transfer* **2017**, *104*, 328-336.
- 458 4. Velram, B.M.; Hamid, S.; Krishnan J.; Debes, B. Mechanical properties of thin films of graphene
459 materials: A study on their structural quality and functionalities. *Current Applied Physics* **2018**,
460 *18*, 879-885.
- 461 5. Allen, M.J.; Tung, V.C.; Kaner, R.B. Honeycomb carbon: a review of graphene. *Chem. Rev.* **2010**,
462 *110*, 132-145.
- 463 6. Voiry, D.; Yang, J.; Kupferberg, J.; Fullon, R.; Lee, C.; Jeong, H.Y.; Shin, H. S.; Chhowalla, M.
464 High-quality graphene via microwave reduction of solution-exfoliated graphene oxide. 2016
465 *Science* **2016**, *353*, 1413-1416.
- 466 7. Huang, X.; Yin, Z.; Wu, S.; Qi, X.; He, Q.; Zhang, Q.; Yan, Q.; Boey, F.; Zhang, H.
467 Graphene-based materials: synthesis, characterization, properties, and applications. *Small* **2011**,
468 *7*, 1876-1902.
- 469 8. Meyer, J.C.; Geim, A.K.; Katsnelson, M.I.; Novoselov, K.S.; Booth, T.J.; Roth, S. The structure of
470 suspended graphene sheets. *Nature* **2007**, *446*, 60-63.
- 471 9. Dong, L.L.; Chen, W.G. Development on preparation, characteristics and application of
472 graphene, *Carbon Tech.* **2016**, *35*, 1-7.
- 473 10. Papageorgiou, D.G.; Kinloch, I.A.; Young, R. J. Mechanical properties of graphene and
474 graphene-based nanocomposites. *Porg. Mater. Sci.* **2018**, *90*, 75-127.
- 475 11. Dong, L.L.; Xiao, B.; Liu, Y.; Li, Y.L.; Fu, Y.Q.; Zhao, Y.Q.; Zhang, Y.S. Sintering effect on
476 microstructural evolution and mechanical properties of spark plasma sintered Ti matrix
477 composites reinforced by reduced graphene oxides. *Ceram. Int.* **2018**, *44*, 17835-17844.
- 478 12. Dong, L.L.; Chen, W.G.; Deng, N. Investigation on arc erosion behaviors and mechanism of
479 W70Cu30 electrical contact materials adding graphene. *J. Alloy. Compd.* **2017**, *696*, 923-930
- 480 13. Fan, F.; Levente, C.; Gyorgy, S.; Christopher, F.B. Robust Covalently Cross-linked
481 Polybenzimidazole/Graphene Oxide Membranes for High-Flux Organic Solvent Nanofiltration.
482 *ACS Appl. Mater. Interfaces* **2018**, *10*, 16140-16147.
- 483 14. Fan, Y.; Jiang W.; Kawasaki, A. Highly Conductive Few - Layer Graphene/Al2O3
484 Nanocomposites with Tunable Charge Carrier Type. *Advanced Functional Materials* **2012**, *22*, 18,
485 3882-3888.

- 486 15. Du, T.; Zhang, H.D.; Fan, T.X. Recent Progress on Graphene/Metal Composites. *Mater. Rev.*
487 **2015**, *29*, 121-129.
- 488 16. Chen, W.G.; Dong, L.L.; Wang, J.J.; Zuo, Y.; Ren, S.X.; Fu, Y.Q. Synergistic enhancing effect for
489 mechanical and electrical properties of tungsten copper composites using spark plasma
490 infiltrating sintering of copper-coated graphene. *Sci. Rep.-UK* **2017**, *7*, 17836-17844.
- 491 17. Liu, G.Z.; Jiang, W.; Sun, D.P.; Wang, Y.P.; Li, F.S. One-pot synthesis of urchinlike Ni
492 nanoparticles/RGO composites with extraordinary electromagnetic absorption properties. *Appl.*
493 *Surf. Sci.* **2014**, *314*, 523-529.
- 494 18. Gotoh, K.; Kinumoto, T.; Fujii, E.; Yamamoto, A.; Hashimoto, H.; Ohkubo, T.; Itadani, A.;
495 Kuroda, Y.; Ishida, H. Exfoliated graphene sheets decorated with metal/metal oxide
496 nanoparticles: Simple preparation from cation exchanged graphite oxide. *Carbon*. **2011**,
497 *49*, 1118-1125.
- 498 19. Ray, A.K.; Sahu, R.K.; Rajinikanth, V.; Bapari, H.; Ghosh, M.; Paul, P. Preparation and
499 characterization of graphene and Ni-decorated graphene using flower petals as the precursor
500 material. *Carbon* **2012**, *50*, 4123-4129.
- 501 20. Zou, Z.Y.; Carnevali, V.; Jugovac, M.; Patera, L.L.; Sala, A.; Panighel, M.; Cepek, C.; Soldano, G.;
502 Mariscal, M.M.; Peressi, M.; Comelli, G.; Africh, C. Graphene on nickel (100) micrograins:
503 Modulating the interface interaction by extended moiré superstructures. *Carbon* **2018**, *130*,
504 441-447.
- 505 21. Eriksson, J.; Puglisi, D.; Kang, Y. H.; Yakimova, R.; Spetz, A.L. Adjusting the electronic
506 properties and gas reactivity of epitaxial graphene by thin surface metallization. *Physica B:*
507 *Condensed Matter*. **2014**, *439*, 105-108.
- 508 22. Hassan, H.M. A.; Abdelsayed, A.; Khder, V.E.R.S.; AbouZeid, K.M.; Turner, J.; El-Shall, M.S.;
509 Al-Resayes, S.I.; El-Azhary, A.A. Microwave synthesis of graphene sheets supporting metal
510 nanocrystals in aqueous and organic media. *J. Mater. Chem.* **2009**, *19*, 3832-3837.
- 511 23. Wang, Y.; Zhao, Y.; Bao, T.J.; Xiang, L.; Su, Y.Q.; Duan, Y.X. Preparation of Ni-reduced graphene
512 oxide nanocomposites by Pd-activated electroless deposition and their magnetic properties.
513 *Appl. Surf. Sci.* **2012**, *258*, 8603-8608.
- 514 24. Kuang, D.; Xu, L.Y.; Liu, L.; Hu, W.B.; Wu, Y.T. Graphene–nickel composites. *Appl. Surf. Sci.*
515 **2013**, *273*, 484-490.
- 516 25. Cao, Y.; Su, Q.M.; Che, R.C.; Du, G.H.; Xu, B.S. One-step chemical vapor synthesis of
517 Ni/graphene nanocomposites with excellent electromagnetic and electrocatalytic properties.
518 *Synthetic Met.* **2012**, *162*, 968-973.
- 519 26. Hummers, W.S.; Offeman, R.E. Preparation of Graphitic Oxide. *J. Am. Chem. Soc.* **1958**, *80* ,
520 1339–1339.
- 521 27. Hirata, M.; Gotou, T.; Horiuchi, S.; Fujiwara, M.; Ohba, M. Thin-film particles of graphite oxide:
522 high-yield synthesis and flexibility of the particles. *Carbon*. **2004**, *42*, 2929-2937.
- 523 28. Tamas, F.; Christos, D.; Jozsef, K.; Gyorgy, T.B.; Peter, H.; Gyorgy, S. Nanofiltration-Enabled In
524 Situ Solvent and Reagent Recycle for Sustainable Continuous-Flow Synthesis. *ChemSusChem*
525 **2017**, *10*, 3435-3444.
- 526 29. Xu, Z.P.; Buehler, M. J. Interface structure and mechanics between graphene and metal
527 substrates: a first-principles study. *J. Phys.: Condens. Matter* **2010**, *22*, 1-5.
- 528 30. Mi, C.T.; Liu, G.P.; Wang, J.J.; Guo, X.L.; Wu, S.X.; Yu, J. First-Principles Calculations of the

- 529 Adsorption of Au, Ag and Cu Atoms on Defected Graphene. *Acta Phys. Chim. Sin.* **2014**, *30*,
530 1230-1238.
- 531
- 532 31. Sun, X. Y.; Wu, R. N.; Xia, R., & Chu, X. H. (2014). Effects of stone-wales and vacancy defects in
533 atomic-scale friction on defective graphite. *Applied Physics Letters* **2014**, *104*(18), 2605.
- 534 32. Zhang, L.; Li, X.; Huang, Y.; Ma, Y.F.; Wan, X.G.; Chen, Y.S. Controlled synthesis of few-layered
535 graphene sheets on a large scale using chemical exfoliation. *Carbon*. **2010**, *48*, 2367-2371.
- 536 33. Terrones, M.; Martín, O.; González, M.; Pozuelo, J.; Serrano, B.; Cabanelas, J.; Vega-Díaz, C. S.
537 M.; Baselga, J. Interphases in Graphene Polymer-based Nanocomposite: Achievements and
538 Challenges. *Adv. Mater.* **2011**, *23*, 5302-5310.
- 539 34. He, H.; Klinowski, J.; Forster, M.; Lerf, A. A new structural model for graphite oxide. *Chem.*
540 *Phys. Lett.* **1998**, *287*, 53-56.
- 541 35. Geim, A.K.; Novoselov, K.S. The rise of graphene. *Nat Mater.* **2007**, *6*, 183-191.
- 542 36. Ferrari, A.C.; Raman spectroscopy of graphene and graphite: Disorder, electron-phonon
543 coupling, doping and nonadiabatic effects. *Solid State Commun.* **2007**, *143*, 47-57.
- 544 37. Fan, X.B.; Peng, W.C.; Li, Y.; Li, X.Y.; Wang, S.L.; Zhang, G.L.; Zhang, F.B. Deoxygenation of
545 Exfoliated Graphite Oxide under Alkaline Conditions: A Green Route to Graphene Preparation.
546 *Adv. Mater.* **2008**, *20*, 4490-4493.
- 547 38. Kudin, K. N.; Ozbas, B.; Schniepp, H. C.; Prud'Homme, R. K.; Aksay, I. A.; Car, R. Raman
548 spectra of graphite oxide and functionalized graphene sheets. *Nano Lett.* **2008**, *8*, 36-41.
- 549 39. Malard, L.M.; Pimenta, M.A.; Dresselhaus, G.; Dresselhaus, M.S. Raman spectroscopy in
550 graphene. *Phys. Rep.* **2009**, *473*, 51-87.
- 551 40. Dong, L.L.; Chen, W.G.; Zheng, C.H.; Deng, N. Microstructure and properties characterization
552 of tungsten-copper composite materials doped with graphene. *J. alloy. Compd.* **2017**, *695*,
553 1637-1646.
- 554 41. Dong, L.L.; Chen, W.G.; Deng, N.; Zheng, C.H. A novel fabrication of graphene by chemical
555 reaction with a green reductant. *Chem. Eng. J.* 2016, *306*, 754 - 762.
- 556 42. Sk, M. M.; Yue, C.; Jen, Y. R. K. Synthesis of graphene/vitamin C template-controlled
557 polyaniline nanotubes composite for high performance supercapacitor electrode. *Polymer*. 2014,
558 55, 798-805.
- 559 43. Hao, Y.; Wang, Y.; Wang, L.; Ni, Z.; Wang, Z.; Wang, R.; Koo, C.K.; Shen, Z.; Thong, J.T. Probing
560 layer number and stacking order of few-layer graphene by raman spectroscopy. *Small*. **2010**, *6*,
561 195-200.
- 562 44. Hontoria-Lucas, C.; López-Peinado, A.J.; López-González, J.D.D.; Rojas-Cervantes, M.L.;
563 Martín-Ar, R.M. Study of oxygen-containing groups in a series of graphite oxides: physical and
564 chemical characterization. *Carbon*. **1995**, *33*, 1585-1592.
- 565 45. Chen, W.F.; Yan, L.F.; Bangal, P.R. Preparation of graphene by the rapid and mild thermal
566 reduction of graphene oxide induced by microwaves. *Carbon*. **2010**, *48*, 1146-1152.
- 567 46. Tian, T.; Tian, N.; Wang, T.; Zhang, B.; Zhang, D.D.; Liu, D.M. In situ chemical reduction
568 method for graphene-copper. *J. Chin. Electr. Microsc Soc.* **2016**, *35*, 404-408.
- 569 47. Lucas, C.; López-Peinado, A.J.; López-González, J.D.D.; Rojas-Cervantes, M.L.; Martín-Ar, R.M.
570 Study of oxygen-containing groups in a series of graphite oxides: physical and chemical
571 characterization. *Carbon*. **1995**, *33*, 1585-1592.

- 572 48. Gao, J.Q.; Wu, Y.T.; Liu, L.; Shen, B.; Hu, W.B. Crystallization temperature of amorphous
573 electroless nickel–phosphorus alloys. *Mater Lett.* **2005**, *59*, 1665-1669.
- 574 49. Hu, Q.H.; Wang, X.T.; Chen, H.; Wang, Z.F. Synthesis of Ni/graphene sheets by an electroless
575 Ni-plating method. *New Carbon Mater.* **2012**, *27*, 35-41.
- 576 50. Fang, J.J.; Li, S.F.; Zha, W.K.; Cong, H.Y.; Chen, J.F.; Chen, Z.Z. Microwave Absorbing
577 Properties of Nickel-coated Graphene. *J. Inorg. Mater.* **2011**, *26*, 467-471.
- 578 51. Jiang, R.G.; Zhou, X.F.; Liu, Z.P. Electroless Ni-plated graphene for tensile strength enhancement
579 of copper. *Mater. Sci. Eng. A.* **2017**, *679*, 323-328.
- 580 52. Ma, E.M.; Luo, S.F.; Li, P.X. A transmission electron microscopy study on the crystallization of
581 amorphous Ni-P electroless deposited coatings. *Thin Solid Films.* **1998**, *166*, 273-280.
- 582 53. Sribalaji, M.; Arunkumar, P.; Babu, K.S.; Keshri, A.K. Crystallization mechanism and corrosion
583 property of electroless nickel phosphorus coating during intermediate temperature oxidation.
584 *Appl. Surf. Sci.* **2015**, *355*, 112-120.
- 585 54. Jiang, R.G.; Zhou, X.F.; Liu, Z.P. Electroless Ni-plated graphene for tensile strength
586 enhancement of copper. *Mater. Sci. Eng. A.* **2017**, *679*, 323-328.
- 587 55. Ning, Z.R.; Chen, Z.; Du, X.J.; Ran, R.X.; Dong, W.P.; Chen, C. Nickel Dimers Adsorbed on
588 Graphene: First-Principle Study. *J. Supercond. Nov. Magn.* **2013**, *26*, 3515-3522.
- 589 56. Laref, A.; Ahmed, A.; Bin-Omran, S.; Luo, S.J. First-principle analysis of the electronic and
590 optical properties of boron and nitrogen doped carbon mono-layer graphene. *Carbon* **2015**, *81*,
591 179-192.
- 592 57. Tang, Y. Z.; Yang, X.M.; Wang, R.R.; Li, M.X. Enhancement of the mechanical properties of
593 graphene–copper composites with graphene–nickel hybrids. *Mater. Sci. Eng. A.* **2014**, *599*,
594 247-254.
- 595